Incorporation, valence state, and electronic structure of Mn and Cr in bulk single crystal β–Ga_2O_3

T. C. Lovejoy,[1,2,a)] Renyu Chen,[2,3] E. N. Yitamben,[1,2,b)] V. Shutthanadan,[4] S. M. Heald,[5] E. G. Villora,[6] K. Shimamura,[6] S. Zheng,[7] S. T. Dunham,[2,3] F. S. Ohuchi,[2,7] and M. A. Olmstead[1,2]

[1]*Department of Physics, University of Washington, Box 351560, Seattle, Washington 98195, USA*
[2]*The Center for Nanotechnology, University of Washington, Seattle, Washington 98195, USA*
[3]*Department of Electrical Engineering, University of Washington, Box 35250, Seattle, Washington 98195, USA*
[4]*Pacific Northwest National Lab, Richland, Washington 99352, USA*
[5]*Advanced Photon Source, Argonne National Lab, Argonne Illinois 60439, USA*
[6]*National Institute for Materials Science, Tsukuba, Japan*
[7]*Department of Materials Science and Engineering, University of Washington, Box 352120, Seattle, Washington 98195, USA*

(Received 11 December 2011; accepted 14 May 2012; published online 25 June 2012)

Single crystals of transition metal (TM) doped β–Ga_2O_3, a wide gap semiconductor system of interest for transparent conductive oxide and diluted magnetic semiconductor applications, have been studied in the dilute, non-interacting limit ($\leq$0.06 cation %). Based on optical absorption, particle induced x-ray emission, and Rutherford backscattering measurements, Mn does not incorporate as well as Cr, and Mn degrades the crystal quality. Using superconducting quantum interference device (SQuID) magnetometry, a Brillouin type paramagnetic magnetization is observed for Mn or Cr doped crystals with an effective number of Bohr magnetons per TM ion of 5.88 ± 0.1 or 3.95 ± 0.1, respectively. A trace ferromagnetic signal is consistent with a very small concentration of secondary phases in the Mn-doped crystal. The position of the edge in x-ray absorption near edge structure (XANES) measurements suggests that the Cr takes the 3+ valence, while a mixture of Mn^{2+} and Mn^{3+} are present; based on the absence of a prominent pre-edge feature in the XANES, both TM predominantly occupy an octahedral site in β–Ga_2O_3. Density functional theory (DFT) results, optical absorption and SQuID data are consistent with this assignment. While the Cr-doped crystal is conductive, the Mn-doped crystal is insulating, which is consistent with the Mn^{2+}/Mn^{3+} mixed valence, assuming the Fermi level is pinned mid-gap at the Mn 2+/3+ transition level, which is predicted by DFT to be 1.8 eV above the valence band maximum. © *2012 American Institute of Physics*. [http://dx.doi.org/10.1063/1.4729289]

I. INTRODUCTION

Transition metal (TM) doping of semiconductors and oxides leads to a number of useful electronic, optical, and magnetic properties. For example, TM-doping at the percent level can lead to diluted magnetic semiconductors (DMS),[1,2] which may someday revolutionize the electronics industry if the Curie temperatures can be engineered to be high enough for widespread technological applications.[3] Both theoretical predictions[4] and experiments[5,6] have shown that Mn-doping in the wide-gap semiconductor GaN can lead to Curie temperatures exceeding room temperature.

Room temperature ferromagnetism has been reported in Ga_2O_3 when doped with Mn to 7–8 cation %.[7,8] In these studies, possibly as a result of the Mn-doping, the Ga_2O_3 takes the spinel-structure γ-polymorph, which is uncommon for the undoped material. On the other hand, Mn-doped Ga_2O_3 on silicon (001) substrates appears to take the monoclinic β-phase (no information was given about the magnetism).[9] The monoclinic β-phase is the only stable form of undoped bulk Ga_2O_3 up to its melting temperature.[10] β-phase-Ga_2O_3 and spinel γ-phase-Ga_2O_3 each possess both tetrahedral and octahedral cation sites, although in different ratios. The monoclinic β-phase has equal concentrations of gallium sites inside oxygen octahedra and tetrahedra, and lattice parameters $a = 12.23$ Å, $b = 3.04$ Å, $c = 5.80$ Å, and $\beta = 103.7^\circ$ (between a and c), see Figure 1. A density functional theory (DFT) study has shown that Mn in β–Ga_2O_3 is more stable in octahedral sites,[11] but the accuracy of these results is questionable due to the high density of Mn-O-Mn bonds, and therefore spurious Mn-Mn interactions, in the very small (20 atom) periodic cell used.

The most detailed information currently available about the state of Mn or Cr TM dopants in the native β–Ga_2O_3 phase comes from electron spin resonance (ESR) or electron paramagnetic resonance (EPR), which measure both the presence and the local site symmetry (through the local spin Hamiltonian parameters) of Mn^{2+} or Cr^{3+} dopants. An ESR study of Mn^{2+} dopants in β–Ga_2O_3 found the site symmetry to be rhombic,[12] while a more recent EPR study found the site symmetry to be only monoclinic.[13] Both studies concluded based on the spectral shape that Mn^{2+} ions occupy a

a)Current address: Nion Co., Kikland, Washington 98033, USA. Electronic address: tlovejoy@uw.edu.
b)Current address: Center for Nanoscale Materials, Argonne National Laboratory, Argonne, Illinois 60439, USA.

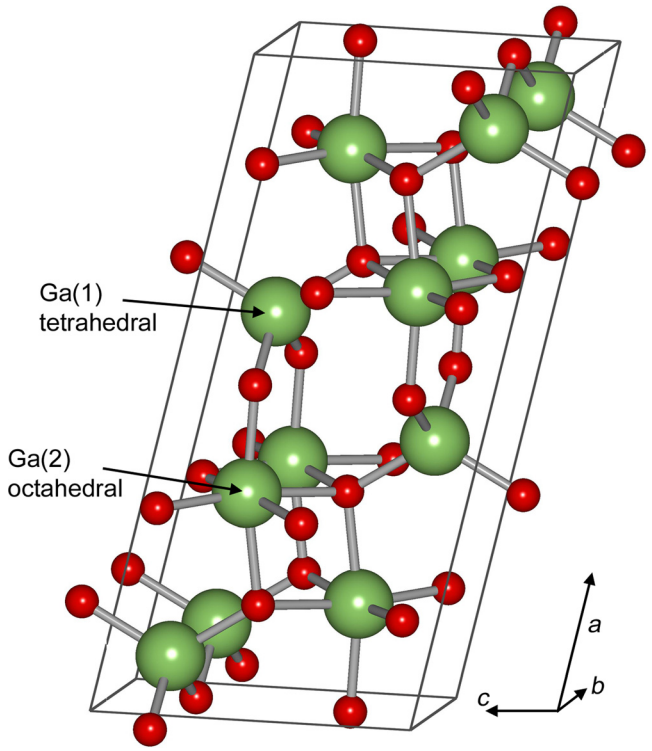

FIG. 1. Simple monoclinic 20 atom cell of β–Ga_2O_3 (twice the primitive cell) showing distorted octahedral and approximately tetrahedral gallium sites. There are three non-equivalent oxygen sites.

single site in the β–Ga_2O_3 lattice; they each proposed this is the octahedrally coordinated Ga^{3+} site based on the closer similarity in ionic radii between Mn^{2+} and Ga^{3+} on octahedral sites than on tetrahedral sites. In γ-phase-Ga_2O_3, on the other hand, x-ray absorption indicates Mn^{2+} occupies the tetrahedrally coordinated Ga site.[7] A significant shortcoming of most EPR spectrometer configurations is that other valence states, such as Mn^{1+} or Mn^{3+}, are not detectable.[13] This makes it difficult to rule out secondary phases, for example, Mn_2O_3, which can give misleading results for dilute magnetism studies. In the related system GaN, combined careful calibration of the Mn^{2+} ESR intensity and independent measurements of the total Mn concentration allowed the Mn^{2+}:Mn^{3+} ratio to be inferred, and even controlled, as a function of doping and temperature.[14,15] A mixed Mn^{2+}/Mn^{3+} population leads to the model shown schematically in Fig. 6, where the Fermi level is located mid-gap at the Mn 2+/3+ transition level, and changes in the Fermi level by more than kT have a large effect on the Mn^{2+}:Mn^{3+} ratio.

From the perspective of potential device application, either as a diluted magnetic semiconductor, luminescent material, or a transparent substrate with controlled conductivity, very little is known about the nature of TM dopants in β–Ga_2O_3 crystals, including which valence states are present and at which sites, and how the electronic structure is affected by the dopants. The goal of this study is to alleviate this situation by presenting a broad perspective on TM (Cr and Mn) doping of β–Ga_2O_3. More emphasis is placed on Mn-doping, but the Cr case is also considered because it is unknown whether Cr-doped Ga_2O_3 can be made magnetic. For example, theoretical and experimental studies have shown that the related system Cr-doped In_2O_3 can be made magnetic through co-doping with Sn.[16,17]

In this article, the atomic, magnetic, and electronic structure of bulk single crystals of Mn-doped and Cr-doped (0.01–0.06 cation %) β–Ga_2O_3 are studied. Based on ion beam techniques, only a small fraction of the TM in the feed material actually incorporates in the Ga_2O_3 lattice. Mn does not incorporate as well as Cr, and Mn incorporation degrades the crystal quality. Based on electron paramagnetic spin resonance (EPR), optical absorption, X-ray absorption near edge structures (XANES), and DFT results, Cr^{3+} is dominant for Cr-doping, while mixed Mn^{2+} and Mn^{3+} are present for Mn-doping; for either TM, the octahedral site occupation dominates. Based on superconducting quantum interference device (SQuID) magnetometry at 5 K, after subtracting a temperature independent diamagnetic component with slope -2.2×10^{-7} emu/gram/Oe, a Brillouin type paramagnetic magnetization is observed for both Cr and Mn doping with an effective number of Bohr magnetons (p_{eff}) 3.95 ± 0.1 and 5.88 ± 0.1, respectively. A trace ferromagnetic component was also observed, but the origin of this signal is unclear in this very dilute system. From electrical measurements, the Cr-doped crystal is conductive, with comparable conductivity to the undoped material, while the Mn-doped crystal appears to be insulating. The latter is consistent with mixed valency if the Fermi level is pinned at the Mn 2+/3+ transition level somewhere in the gap. DFT results support this picture and predict the 2+/3+ level to be located 1.8 eV above the valence band maximum (VBM).

II. EXPERIMENTAL DETAILS

Undoped, Mn-doped, and Cr-doped single crystals of β–Ga_2O_3 were grown by the floating zone technique at the National Institute for Materials Science (NIMS) in Tsukuba, Japan.[18] For undoped samples, powders of 99.99% pure Ga_2O_3 were sintered into feed rods several cm in length and about one cm in width. No intentional dopant was added, although Si is known to be an impurity in the Ga_2O_3 system.[18] For the Mn-doped sample, 0.2 mol. % MnO_2 powder was mixed in with the starting material before sintering; Cr_2O_3 was added for the Cr-doped samples.[36] After making connection to a seed crystal at the beginning of the rod, the feed rods were slowly lowered through the focal point of two intense lamps to crystallize the material. In the undoped or Cr-doped cases, this resulted in a transparent crystal with uniform color along its length of slightly bluish color or greenish color, respectively. For the Mn-doped case, the resulting transparent crystal exhibited a gradient of a pinkish tint along the growth direction from most clear near the seed side (the beginning), to most pink near the end. For the measurements below, crystals were cleaved with a sharp blade along the (100) and (001) planes to expose a (100) surface $\sim 3 \times 5$ mm^2 and $\sim$1 mm thick. The (010) is more difficult to cleave, but the dimension of the as-grown crystals along (010) was already convenient for measurement.

Rutherford backscattering (RBS) and particle induced x-ray emission (PIXE) measurements were conducted at the Environmental Molecular Science Laboratory (EMSL) located at Pacific

Northwest National Lab. For channeling experiments, a 2.0 MeV He^+ excitation was used, and the RBS or PIXE yield was measured as a function of sample tilt within a few degrees of normal incidence; backscattered He was measured at 150° off the beam direction (RBS channeling), and x-ray emission was measured 145° off the beam direction (PIXE channeling). χ_{min} is the minimum yield in the channeling direction near normal divided by the yield in a random direction about 1° off channeling. Typical values of χ_{min} from RBS range from ~2% for single crystal silicon to ~100% for an amorphous material. For atomic concentrations, PIXE was used with a 2.555 MeV H^+ excitation. The incident direction was +45° off normal, and the x-ray detector was −36° off normal. Atomic concentrations were determined by fitting data collected from standards and the samples using the program GUPIXWIN.[19]

X-ray absorption measurements were conducted at the advanced photon source (APS) sector 20BM PNC/XOR-CAT. Single crystal samples were mounted on spinners and rotated about the sample normal at about 3 Hz during measurement where x-rays polarized near the plane of the sample impinged at grazing incidence (2°–3°). The x-ray energy was scanned through the Mn or Cr K-edge energies, and the K-edge fluorescence was captured from near the plane of the sample (~5°) with a liquid nitrogen cooled, 13 element Ge detector. The reference compounds were powdered and measured in transmission.

Optical absorption measurements employed a Cary 500 scan UV-ViS-NIR spectrophotometer to measure transmission of unpolarized light incident normal to the (100) plane. EPR measurements used a commercial X-band Bruker E580 spectrometer. SQuID measurements using a Quantum Design MPMS-5 S magnetometer were conducted on samples cleaved on four sides with a ceramic blade and held in the sample mount by its elastic tension. The sample mount was a fresh, visually flawless drinking straw. The orientation of the sample was such that the sample moment was measured along the [001] direction, which lies in the (100) plane of the sample.

Spin polarized DFT calculations were carried out using the generalized gradient approximation (GGA PW91)[21] within the Vienna *ab initio* simulation package (VASP).[22,23] To avoid spurious TM-TM second neighbor interactions, a 40 atom supercell of β–Ga_2O_3 was used with dimensions $\sim 1.2 \times 0.6 \times 0.6$ nm^3. This corresponds to doubling the cell shown in Fig. 1 along the *b* direction. For the band structure plots (Fig. 5), the paths through the Brillouin zone (BZ) of the 40 atom supercell are labeled in terms of its reciprocal lattice vectors *a**, *b**, and *c**. The path through the BZ is a line parallel to *c** from *c**/2 to Γ followed by a rectangle starting with a line parallel to *b** from Γ to *b**/2 and ending with a line parallel to *a** from *a**/2 to Γ. The BZ for the primitive cell of β–Ga_2O_3 is shown in Ref. 20.

III. RESULTS

The coloration gradient in the Mn-doped sample correlates to an increase in Mn concentration and a decrease in crystal quality. Table I shows the atomic concentrations measured by PIXE and the χ_{min} values determined by RBS for the undoped crystal, the Cr-doped crystal, and the Mn-doped crystal. Three samples were taken from the Mn-doped crystal: one from each of the beginning (closest to seed), where the sample is the lightest pink, middle, and end, where the sample is darkest pink. Table I shows that increasing distance from the seed corresponds to an increase in Mn concentration from 0.01 to 0.025 cation %. The Cr-doped sample is more heavily doped with ~0.06 cation % Cr. With χ_{min} between 16% and 18%, the undoped and Cr-doped crystals have about the same degree of order. The Mn-doped crystal, on the other hand, has much higher χ_{min} despite having lower doping. The relatively high χ_{min} values further increase as the Mn concentration increases from the beginning to end of the crystal, which indicates a correlation between increasing Mn content and disorder. The value of χ_{min}, even in the undoped crystal, is higher than expected since a single crystal of silicon has χ_{min} around 2%.

TABLE I. Transition metal concentrations from PIXE and crystal quality parameter from RBS (χ_{min}) for undoped crystal, Cr-doped crystal, and Mn-doped crystal at three points along color gradient. Mn concentration correlates inversely with crystal quality, but Cr does not.

Crystal	TM concentration (cation %)	χ_{min}
Undoped	–	18%
Cr	0.058%	16%
Mn—beginning	0.010%	48%
Mn—middle	0.023%	54%
Mn—end	0.025%	68%

To gain an understanding of the element specific crystal ordering, PIXE channeling measurements were conducted on the Cr-doped and Mn-doped (0.023%) samples. In the Cr-doped case, the channeling (minimum) PIXE yield was about 50% of random for both Cr and Ga. Whereas in the Mn-doped case, the channeling PIXE yield was about 70%–80% for Mn and ~75% for Ga. Low Mn concentration and sample charging led to relatively high noise levels, even for long acquisition times, in the Mn-doped case. In general, similar channeling yield for dopants compared with primary elements indicates that the dopants occupy specific, probably substitutional, lattice sites. Due to the higher intrinsic minimum in PIXE channeling yield, RBS channeling and PIXE channeling results cannot be compared quantitatively.

Optical absorption spectra of Cr-doped, Mn-doped (0.023 cation %), and undoped Ga_2O_3 are shown in Fig. 2. β–Ga_2O_3 has an anisotropy in the optical band gap where the gap is different, 4.5 eV or 4.8 eV, for light linearly polarized along (001) or (010), respectively.[24] For normal incidence unpolarized light and (100) oriented samples, as used in Fig. 2, the 4.5 eV gap appears as shoulder in each spectrum before the 4.8 eV gap absorption saturates the measurement. Other than the gap absorption, the spectrum for the undoped sample has no major features in the band gap. In addition to the gap absorption, the spectrum from the Cr-doped sample also exhibits two clear peaks at 2.0 and 2.9 eV, see Fig. 2 (inset). This is the origin of the green color. The spectrum from the Mn-doped sample exhibits a peak at 2.6 eV, which corresponds to the pink/red color. The Mn spectrum also has

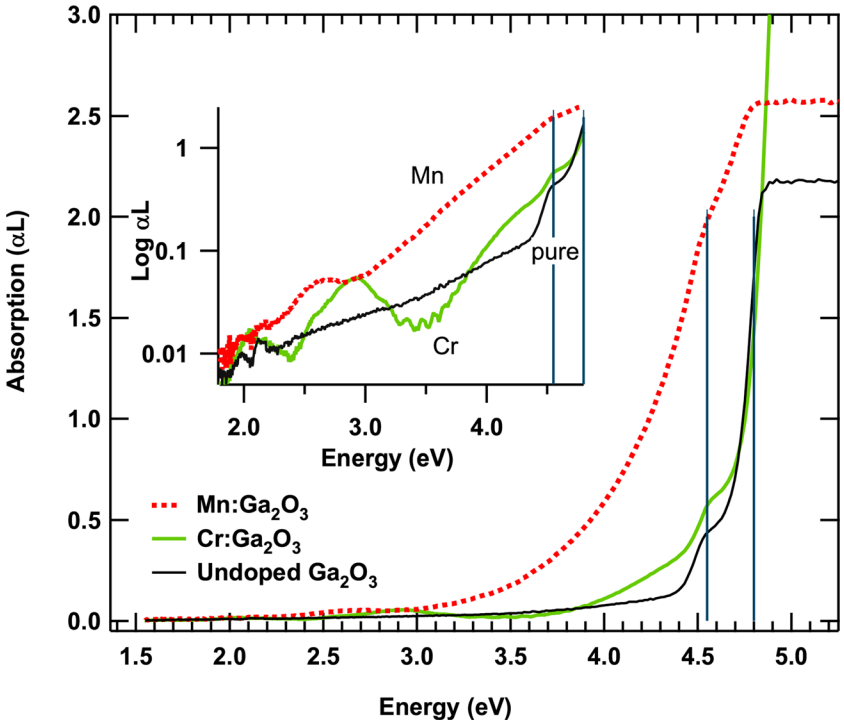

FIG. 2. Optical Absorption spectra for undoped, Mn-doped, and Cr-doped β–Ga_2O_3 single crystals. Black vertical lines mark the optical gap for each linear polarization.(inset) The same data plotted with a log scale on the vertical axis.

a much wider tail stretching from about 3 eV to the band gap absorption at 4.8 eV that almost obscures the 4.5 eV gap absorption.

K-edge XANES was conducted to determine the local environments and valence states of the transition metal dopants in β–Ga_2O_3. Figure 3(a) shows the XANES spectra for Cr-doped Ga_2O_3 and several other Cr-containing compounds with varying Cr valence. The position of the absorption edge of Cr in Ga_2O_3 is indistinguishable from that in Cr_2O_3 and neither exhibits a significant pre-edge peak. Figure 3(b) shows the XANES spectra for Mn-doped Ga_2O_3 and several reference compounds with Mn in increasing formal valence (oxidation) state. The position of the edge in Mn-doped Ga_2O_3 (red/dark solid) is intermediate between that of MnO and Mn_2O_3 but corresponds closely with Mn_3O_4. Similar to the Cr-doped case, the Mn:Ga_2O_3 XANES spectrum shows little or no pre-edge peak intensity. For examples of XANES spectra with significant pre-edge peak intensity, which is

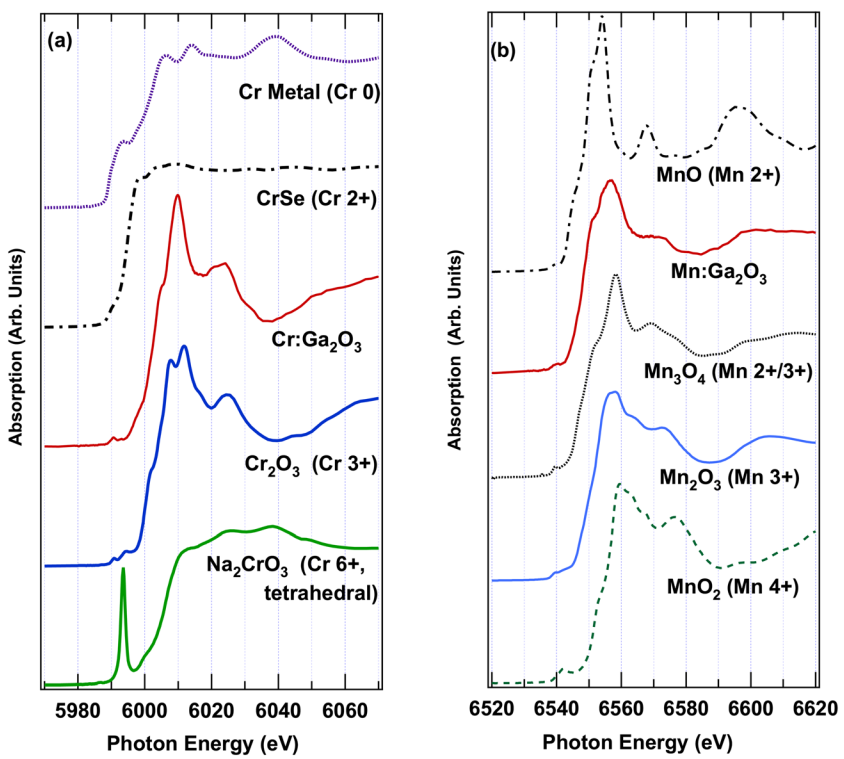

FIG. 3. K-edge XANES for (a) Cr-doped Ga_2O_3 and various Cr-containing compounds with varying Cr valence, and (b) Mn-doped Ga_2O_3 and several reference compounds (MnO, Mn_3O_4, Mn_2O_3, MnO_2) with various Mn valence (2+ thru 4+).

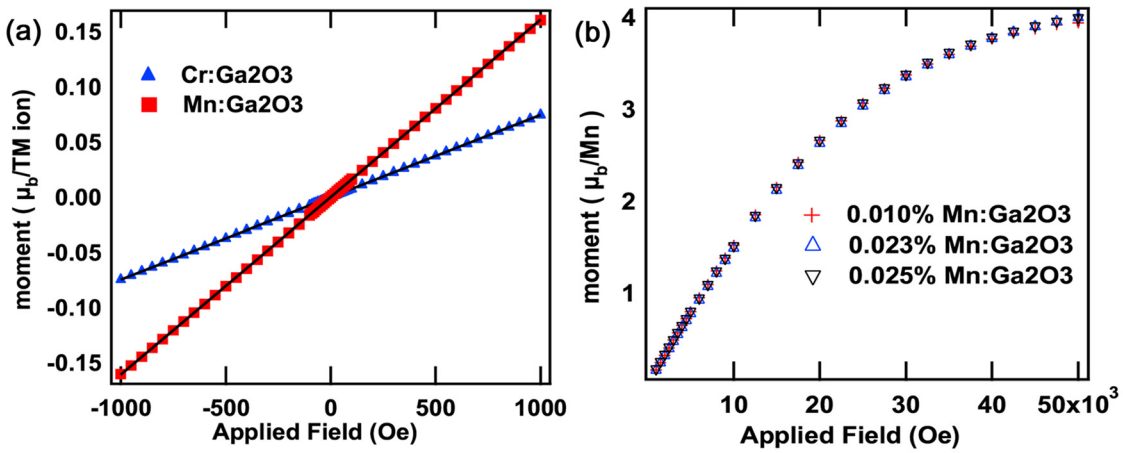

FIG. 4. Magnetic moment in μ_b/TM ion from SQuID at 5 K vs applied field for (a) Mn (red squares) and Cr (blue triangles) from 1000 Oe to −1000 Oe to 1000 Oe (loop), and (b) Mn samples from beginning, middle, and end of the crystal (increasing Mn) from 1000 Oe to 50,000 Oe (5 T). The curves in (b) are almost exactly overlapping. A linear diamagnetic contribution has been subtracted.

indicative of a non-centrosymmetric environment (e.g., tetrahedral sites), one can refer to the literature for Cr and for Mn in GaN.[25,26]

The magnetic susceptibilities of the transition metal dopants in Ga_2O_3 were probed with SQuID magnetometry. At 300 K, the dominant contribution was a linear diamagnetic component with a slope of negative 2.2×10^{-7} emu/gram/Oe. The same value was also observed in the undoped samples. At low temperature (5 K) and low fields ($\leq$1000 Oe), the dominant contribution after subtracting the diamagnetic component (assumed the same at 5 K as 300 K) was a linear Brillouin type paramagnetic component as shown in Fig. 4(a). Using the TM concentration from PIXE and the sample mass to determine the number TM atoms in each sample, a linear fit to a Brillouin function in the small field limit,[27]

$$\frac{m}{B} = \frac{p_{eff}^2 \mu_b^2}{3k_b T},$$

gives $p_{eff} = 3.95 \pm 0.1$ for Cr:Ga_2O_3 and $p_{eff} = 5.88 \pm 0.1$ for Mn:Ga_2O_3, where p_{eff} is the effective number of Bohr magnetons per TM ion. Figure 4(b), which shows the high-field ($\leq$5 T) paramagnetic saturation at 5 K for samples with 0.010% Mn, 0.023% Mn, and 0.025% Mn, as determined by PIXE (see Table I), after subtracting the per-gram diamagnetic signal and normalizing by Mn content. The curves are almost identical. This puts a lower bound on the saturation value of 4.0 μ_b/Mn because we were unable to measure out onto the flat, saturated, region of the curve due to the instrument's maximum field being only 50×10^3 Oe (5 T). Error bars on the data points would be set by the imprecision in measuring the sample mass, which vary from as low as ~3% for the middle samples (0.040 ± 0.001 g) to as high as 20% for the end sample because it was very small (0.005 ± 0.001 g),

After subtracting a linear background to remove both paramagnetic and diamagnetic contributions, a small hysteresis curve remained at both 5 K and 300 K. We measured only a minor loop inside the major hysteresis curve. So, we put lower bounds on the saturation magnetization, remanence, and coercive fields of 0.001 μ_b/Mn, 0.0008 μ_b/Mn, and 250 Oe, respectively, for the 0.01% doped Mn crystal. In the Cr case, the remanence was about 10 times smaller.

EPR spectra on the 0.025% Mn-doped sample showed a five-line fine structure and six hyperfine lines, similar to that reported previously for Mn in β–Ga_2O_3.[12,13]

The electrical conductivity of the various samples may provide clues to the nature of the TM dopant. However, one must be cautious in drawing conclusions based on the measured electrical conductivity of β–Ga_2O_3 crystals because non-ohmic contacts are commonplace, apparently due to oxygen-induced surface band bending.[28] Also, the origin of the conductivity is not well understood, even in the undoped material. It is known that evaporating Ti followed by Au,[29] or applying molten Sn followed by high voltage treatment,[20] can make ohmic contacts to undoped Ga_2O_3. Using Ti/Au contacts, the Cr-doped and undoped crystals were conductive (~20 Ω^{-1} cm^{-1}),[29] while the Mn-doped crystal was completely insulating. We conclude that the Mn-doped crystal is insulating. However, it is possible that making ohmic contacts to Mn-doped β–Ga_2O_3 is substantially different or more difficult than to undoped β–Ga_2O_3. Charging artifacts were observed in the Mn-doped crystals with ion beam and photoemission techniques, but not in the Cr-doped and undoped samples, which further supports the conclusion that the Mn-doped crystal is insulating.

To understand the impact of the TM dopants on the electronic structure, the electronic structure of pure and TM-doped β–Ga_2O_3 was computed with DFT. The calculated band structure of pure β–Ga_2O_3 is shown in Fig. 5(a), plotted in the supercell Brillouin zone, which is 1/4 the size of the primitive Ga_2O_3 zone. There is thus considerable zone folding relative to the primitive BZ, but this size unit cell is required to minimize interactions between TM dopants. There is a series of valence bands from the VBM at 0 eV (the energy reference) down to about −7 eV. There are no states in a band gap of width 2.13 eV (calculated conduction band minimum (CBM) at Γ) above the VBM. The calculated DFT:GGA band gap of 2.13 eV is less than half the experimental values of 4.5–4.9 eV, with the discrepancy presumably being due to the well-known band gap estimation error

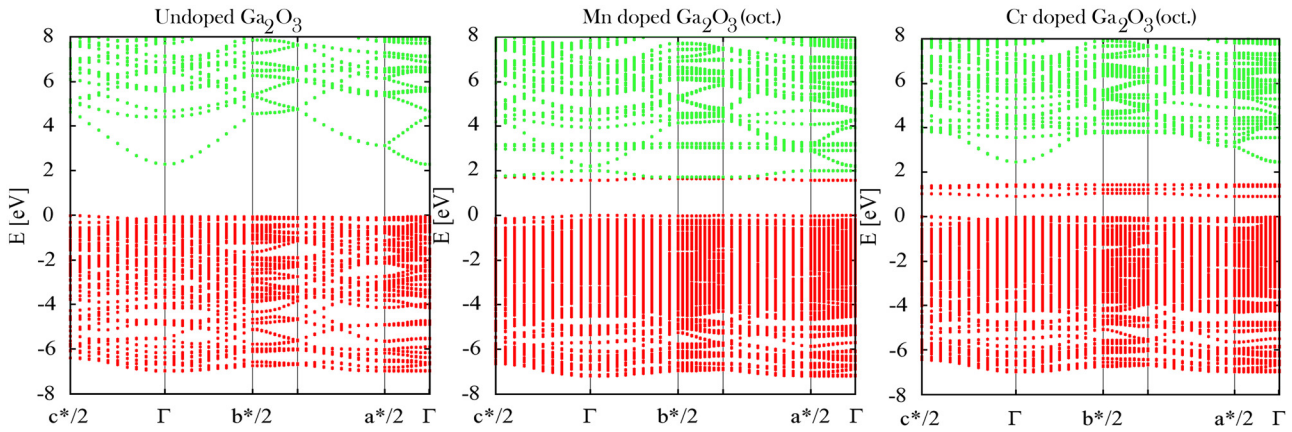

FIG. 5. DFT:GGA band structure plot for relaxed, neutral, 40-atom cell of (a) undefected β–Ga_2O_3 (b) β–Ga_2O_3 with one Mn replacing an octahedral Ga and (c) one Cr atom replacing an octahedral Ga. Filled states are shown in red dots (darker) and unfilled states in green dots (lighter).

of DFT within the GGA. As discussed in our previous work,[30] except for the gap, there is reasonable agreement between the bands produced by DFT:GGA and experimental mapping of the occupied states with angle resolved photoemission. Subsequent experimental and DFT comparisons have given qualitatively similar results, but better quantitative agreement, most notably by using hybrid functional DFT calculations, which include a free parameter, the Hartree-Fock exchange interaction mixing ratio, to fit the experimental band-gap.[20] No experimental data exists for the dispersion of the unoccupied states in the conduction band (CB). The DFT:GGA results show a single low-energy state that disperses up from the zone center, with the next CB state about 4.5 eV above the VBM, followed by a series of relatively closely spaced bands with increasing energy.

Total energy density functional theory calculations were done to study the site occupancy of the dopants. Comparing the total energy of relaxed, neutral, 40-atom supercells with the TM dopant occupying the tetrahedral or octahedral gallium site reveals that the octahedral site is energetically favorable for both dopants. The octahedral site is 1.57 eV lower in energy for Cr, and 0.63 eV lower for Mn.

The new electronic states caused by Mn or Cr doping of β–Ga_2O_3 were studied with DFT. For both dopants, new states appear within the band gap of the pure material. Because octahedral site occupancy is found energetically stable, the effect of the dopants in octahedral sites is emphasized. Figure 5(b) shows the electronic band structure for the 40 atom supercell with one Mn dopant replacing a gallium in an octahedral site. Relative to pure β–Ga_2O_3, there are two new bands within the band gap occupying energies between 1.5 eV and 2 eV. For the neutral cell, which corresponds to 3+ valence for the Mn, one of these new states is occupied [dark color (red) in Fig. 5(b)], and the other unoccupied. Figure 5(c) shows the band structure for a Cr dopant on an octahedral site. There are three new bands within the band gap occupying energies between 1 eV and 1.5 eV. Unlike the Mn case, for the Cr case, all the mid-gap states are filled for neutral cell (Cr^{3+}). For both dopants, new bands also appear within the valence and conduction bands.

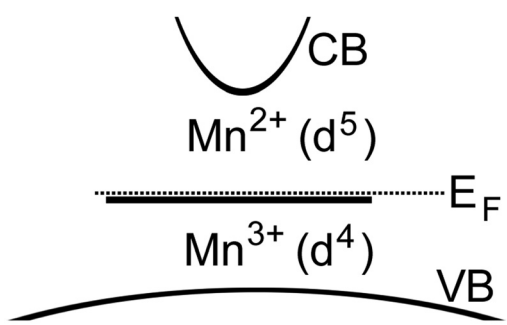

FIG. 6. Schematic diagram showing mid-gap Fermi level near the Mn^{2+}/Mn^{3+} transition level.

IV. DISCUSSION

The valence state and site occupancy of TM dopants are among the basic and fundamental considerations in understanding the material properties imparted by the dopant. X-ray absorption, optical absorption, magnetometry, ion beam techniques, and DFT calculations give consistent, complementary information about the valence state, site occupancy, and the effect on the electronic structure of the TM dopants in β–Ga_2O_3. Given the similarity in metal-oxygen bond length between Ga_2O_3 and Cr_2O_3, one might expect Cr to replace Ga and take 3+ valence. It is not trivial to predict how Mn, which often takes Mn^{2+} valence ($4s^2 3d^5$), will incorporate into the Ga_2O_3 lattice.

A. Valence state

The various techniques employed here give a consistent picture that Cr is present in the 3+ valence state, while both Mn^{2+} and Mn^{3+} are present.

The Mn and Cr K-edge XANES gives a measure of the valence state of the TM dopants. The valence state is determined by comparing the edge positions to reference compounds with known valence. The Cr edge is similar in position to Cr_2O_3, so, it is assigned to Cr^{3+}. The Mn is assigned to mixed Mn^{2+}/Mn^{3+} valence due to the edge position being intermediate between MnO and Mn_2O_3. The edge position is close to that of Mn_3O_4, which has mixed valence of Mn^{2+} and Mn^{3+} in a 2 to 1 ratio.

The slopes of the magnetization curves at low temperature (5 K) and fields ($\leq$1000 Oe) also suggest the presence of Cr^{3+} but indicate a predominance of Mn^{2+}. The slope of the curve gives an "effective number of Bohr magnetons" (p_{eff}), which is a signature of the valence state of the TM based on the model of frozen orbital spins. For Cr^{3+} and Cr^{2+} the expected p_{eff} are 3.8 and 4.9, respectively.[27] The measured value for Cr:Ga_2O_3 (3.95 ± 0.1) is consistent with Cr^{3+}. The expected p_{eff} are for Mn^{3+} and Mn^{2+} are 4.9 and 5.9, respectively. The measured value for Mn (5.88 ± 0.1) suggests a strong predominance of Mn^{2+}. This Mn^{2+}:Mn^{3+} ratio is different from that suggested by XANES. This could be due to a depopulation of the Mn^{3+} at 5 K, or to a fundamental difference between the two techniques. The simple frozen orbital model used to attribute an exact charge state to a partly covalent system may not be sufficient to understand the difference between these two measurements.

The optical absorption spectrum of Cr-doped Ga_2O_3 exhibits the characteristic, identifying feature of trivalent Cr^{3+} in an octahedral ligand field. The absorption spectrum associated with Cr^{3+} octahedrally coordinated by oxygen is very well known from the related system Cr-doped Al_2O_3 (ruby). Relative to ruby, the average position of the absorption lines are very similar, but the bands are broadened and shifted slightly to lower energy,[31] which explains the green color of Cr:Ga_2O_3, while ruby is red. As with ruby, a strong red luminescence makes Cr:Ga_2O_3 a good candidate as a laser medium; this has been known for a long time[31] but does not appear to have ever been implemented, despite some possible advantages over the more common materials like ruby.[32]

The optical absorption of Mn-doped Ga_2O_3 can also be used as a signature of trivalent Mn^{3+} in an octahedral ligand field but does not rule out the presence of Mn^{2+}. Mn^{2+} absorption is typically very weak because the transition to the lowest excited state is dipole-forbidden (a spin flip is required). Therefore, for dilute systems, Mn^{2+} can be considered optically transparent—at least in that it imparts no color. Thus, the pinkish tint in Mn-doped Ga_2O_3 can be recognized immediately as the signature of octahedral Mn^{3+}. A peak in the absorption spectrum located at 2.6 eV is visible in Fig. 2; the energy of this peak agrees quantitatively with the peak position in Mn^{3+} octahedrally coordinated by water,[33] for example. Mn^{3+} in a tetrahedral field has a characteristic absorption peak around 1.5 eV, as in GaN, for example,[34] which is not observed here. The tail on the band gap in the optical absorption in the Mn-doped crystal may be due to the increased crystal disorder, or to absorption between one of the band edges and the Mn^{2+} level.

In contrast to the optical absorption, the EPR signal can be used as a characteristic, identifying feature of Mn^{2+} in the lattice but does not rule out the presence of Mn^{3+}. The five-line fine structure and six hyperfine lines observed are often used as a characteristic feature of Mn^{2+} in EPR.[13] On the other hand, for many EPR spectrometers (including the one used here), Mn^{3+} cannot be detected because the particular combinations of available magnetic fields and excitation frequencies will not excite the resonance of Mn^{3+}.

In summary, XANES, magnetization, and optical absorption suggest the presence of Cr^{3+} in the Cr-doped crystal. The picture is more complicated for the Mn-doped crystal: EPR suggests the presence of Mn^{2+} but does not rule out Mn^{3+}; optical absorption is just the opposite suggesting the presence of Mn^{3+} while not ruling out Mn^{2+}; XANES suggests both are present in a roughly 2 to 1 ratio. Magnetization data suggest Mn^{2+} is dominant at 5 K.

B. Site occupancy

The site occupancy can be determined from the intensity of the pre-edge feature in x-ray absorption (before the main absorption) and ion beam techniques, which gives a consistent assignment with the optical absorption data. Non-centrosymmetric site occupancy, like at tetrahedral sites, in Mn and Cr compounds causes an intense pre-edge feature.[25,26] Such a feature is not observed in Fig. 3(a) or 3(b), so we conclude the TM occupy centrosymmetric sites, such as octahedral sites. The ion beam techniques RBS and PIXE show that the increased Mn incorporation degrades the crystal quality but suggests that Mn and Cr probably occupy substitutional lattice sites. This implies that the majority of the Mn does not participate in secondary phases. Ga_2O_3 exhibits equal numbers of octahedral and tetrahedral Ga sites; these results suggest that Cr and Mn preferentially occupy the octahedral site.

Octahedral site occupation by both dopants is also supported by DFT calculations. The octahedral site is 0.63 eV (1.57 eV) lower in energy for Mn (Cr). This result agrees qualitatively with the XANES data in suggesting that the octahedral site should be dominant. This is also consistent with previous site assignment from ESR based on ionic size arguments.[12,13]

C. Solubility

The incorporation and solubility of Cr and Mn into Ga_2O_3 are quite different. The Cr concentration is uniform, although lower than that in the starting melt. Mn, on the other hand, incorporates at a concentration well below that in the starting material and increases as the growth proceeds. We propose that due to Mn's low solubility, unincorporated Mn accumulates at the growth front, which results in an increased Mn concentration there. As growth continues, the amount of Mn that is incorporated increases due to the higher concentration at the growth front. This behavior is not observed for Cr, which suggests the incorporation is much more likely, and that the solubility is higher. For either dopant, the decreased dopant concentration in the final crystal relative to the starting melt is explained by the purifying effect of the float zone method–the undissolved atoms are swept out of the crystal.

A plausible reason for the higher solubility, easier incorporation, and better crystal quality of the Cr compared the Mn is the similar valence between the Cr^{3+} dopant and the Ga^{3+} lattice site versus the dissimilar valence between Mn^{2+} and Ga. Incorporation of a dopant with different valence state requires atomic and electronic rearrangements, which

would cause a decrease in the crystal quality. This is consistent with the ion beam results.

The small hysteresis observed with magnetometry is not attributed to ferromagnetic interactions between the highly dispersed Mn. It is more likely that a very small fraction (<0.001) of the Mn participates in some secondary phase with complex magnetic properties that give rise to this signal. The Mn-Mn distance, assuming uniform dispersion throughout the crystal, at 0.025 cation % is ~5 nm, presumably much larger than the magnetic interaction length in this highly resistive sample. A small amount of secondary phases may also contribute to the high on-axis ion scattering in the Mn-doped crystal. If they are present, secondary phases such as MnGa and Mn_3O_4 could give rise to such a hysteresis signal.

D. Electronic structure

Before drawing conclusions based on DFT results, it is necessary to carefully consider two important practical limitations of DFT. First, one must extrapolate the changes in electronic structures from the high dopant concentration (~6 cation %) used in the DFT work, caused by using a computationally tractable 40 atom supercell, down to experimentally relevant concentrations (≤0.06 cation %). Second, one must consider the well-known band-gap underestimation problem of DFT, which is especially important for β–Ga_2O_3 where DFT with the GGA underestimates the band gap by more than a factor of two. Regarding the former, assuming uniform distribution of the dopants, the very low dopant density in the experiment is insufficient to produce energy dispersing bands in the band structure. Isolated, localized, and thus nondispersing, defect states are expected instead. It is reasonable to expect the isolated defect states to have energies similar to the defect bands. This methodology has been applied successfully to the study of defects and impurities in oxides and nitrides; for a review see Ref. 35. The band-gap underestimation issue is, at present, fundamental to DFT–there exists no general recipe how to correct the band gap in a way that is guaranteed to also give correct energies for the all the various possible defect states within the gap. Despite the quantitative error in the band gap, DFT with the GGA results are likely to agree qualitatively with the experiment. That is, defects states located within the experimental band gap can be expected to show up within DFT band gap in the calculations. As a result, we restrict ourselves to drawing only qualitative conclusions from the DFT and refer to the experiments for quantitative information.

With the above caveats in mind, the DFT results provide a partial theoretical framework for predicting how the defects affect the material properties, especially with regard to the electrical conductivity. In practice, controlling the carrier concentration and doping type (*p*- or *n*-) of Ga_2O_3 is not well understood; even very pure Ga_2O_3 often exhibits *n*-type conductivity, while *p*-type Ga_2O_3 remains elusive. The calculations employed a neutral cell, with the dopant substituting for Ga, and therefore with an effective valence state of 3+ (equal to the Ga it replaced) for either dopant. Considering the Cr-doped case, the mid-gap defect states of the Cr^{3+} are all filled [see Fig. 5(c)] and are thus unlikely to have any effect on the electronic properties of the *n*-type material because the mid-gap states are far from the Fermi level. In the Mn-doped case, the mid-gap defect states of Mn are half occupied for the neutral cell (Mn^{3+}); that is, the Fermi level is located in between two defect states. Filling the next state corresponds to putting another electron on the Mn defect, and thus decreasing the valence to 2+. This identifies the energy mid-point between these two defect states as the 2+/3+ transition level, see Fig. 5(b). The Mn-doped crystal can only exhibit *n*-type (*p*-type) conductivity if extra electrons are added (removed) by some other dopant in such concentration to fill (empty) all the Mn mid-gap defect states; this would also cause the Mn valence state to decrease (increase). In other words, if Mn doping is the dominant defect in the β–Ga_2O_3 crystal, the Fermi level will be pinned mid-gap at the energy of the Mn 2+/3+ transition level. DFT with the GGA puts this energy roughly 1.8 eV above the VBM in the (underestimated) 2.1 eV band gap. It is reasonable to expect that the qualitative features of the DFT:GGA results also apply in the actual system with the true band gap; that is, we can expect similar, experimentally significant Mn-induced gap states well removed from both the CB and VB of Mn-doped β–Ga_2O_3.

For the Mn-doped crystal, the experimental observation that both charge states (2+ and 3+) are occupied, together with the high resistivity, show that the Fermi level is both located within *kT* of the 2+/3+ transition level, and far (many *kT*) from either band edge. This experimental situation is depicted schematically in Fig. 6. In this model, if the Fermi level were higher, more electrons would enter the Mn *d*-shell and the Mn^{2+}:Mn^{3+} ratio would increase. Thus, this model makes a prediction that co-doping with silicon, for example, would increase the relative amount of Mn^{2+}. This is similar to the situation reported for Mn-doped GaN.[14,15] This experimental picture is exactly consistent with, but not dependent upon, the prediction from the DFT calculations. It is possible that the long tail in the Mn absorption spectra is due to the excitation from the valence band maximum to E_F, or from E_F to the conduction band minimum. The tail has an onset around 3 eV, which suggests that the VBM is either ~3 eV below E_F, or that the CBM is ~3 eV above. In either case, E_F is within 1 eV of the center of the 4.8 eV band gap. An alternate theory is that the tail in the absorption arises from the increased local disorder caused by the Mn, which could create an abundance of electron traps inhibiting conduction. Whatever the mechanism, doping with Mn may provide a convenient and reliable method of obtaining very insulating β–Ga_2O_3 crystals, a feat which is otherwise complicated by the fact that the origin of the conductivity in this material is not well understood.

V. CONCLUSION

In summary, Mn (pinkish) and Cr (green) doped β–Ga_2O_3 single crystals have been studied. Based on RBS and PIXE results, the Mn does not incorporate as well as the Cr, and Mn degrades the crystal quality. Based on XANES, EPR, optical absorption, SQuID measurements, and DFT

calculations Mn exists in both 2+ and 3+ formal oxidation states, while Cr only takes the 3+ state; both TMs preferentially occupy the octahedral cation site in β–Ga_2O_3. A likely explanation for the superior incorporation and crystal quality of the Cr compared to the Mn is similar valence state of the Cr^{3+} and Ga^{3+}. On the other hand, Mn takes mixed valence between 2+ and 3+, which requires electronic and atomic reconstruction to incorporate into the lattice. The high resistivity and the mixed valence of the Mn suggest that the Fermi level is pinned mid-gap at the Mn 2+/3+ transition level; DFT calculations predict the 2+/3+ transition level to occur ~1.8 eV above the VBM.

ACKNOWLEDGMENTS

Work was supported in Seattle by the NSF (Grants Nos. DMR-0605601 and DMR-0710641), and at the Advanced Photon Source by the DOE under Contract No. DE-AC02-06CH11357. TCL acknowledges an IGERT Traineeship from NSF/NCI DGE 0504573 through the UW Center for Nanotechnology. The ion beam work at EMSL was sponsored by the Department of Energy's Office of Biological and Environmental Research. The authors acknowledge S. T. Ochsenbein for his help taking and analyzing the optical absorption and EPR data. The computational part of this research was performed on a computing cluster provided via donations from Intel, AMD, and NSF Grant No. EIA-0101254, as well as computational resources from EMSL, a user facility sponsored by the Department of Energy's Office of Biological and Environmental Research.

[1]H. Ohno, A. Shen, F. Matsukura, A. Oiwa, A. Endo, S. Katsumoto, and Y. Iye, Appl. Phys. Lett. **69**, 363 (1996).
[2]H. Ohno, Science **281**, 951 (1998).
[3]S. Wolf, D. Awschalom, R. Buhrman, J. Daughton, S. Von Molnar, M. Roukes, A. Chtchelkanova, and D. Treger, Science **294**, 1488 (2001).
[4]T. Dietl, H. Ohno, F. Matsukura, J. Cibert, and D. Ferrand, Science **287**, 1019 (2000).
[5]M. L. Reed, N. A. El-Masry, H. H. Stadelmaier, M. K. Ritums, M. J. Reed, C. A. Parker, J. C. Roberts, and S. M. Bedair, Appl. Phys. Lett. **79**, 3473 (2001).
[6]S. Sonoda, S. Shimizu, T. Sasaki, Y. Yamamoto, and H. Hori, J. Cryst. Growth **237–239**, 1358 (2002).
[7]H. Hayashi, R. Huang, H. Ikeno, F. Oba, S. Yoshioka, I. Tanaka, and S. Sonoda, Appl. Phys. Lett. **89**, 181903 (2006).
[8]R. Huang, H. Hayashi, F. Oba, and I. Tanaka, J. Appl. Phys. **101**, 063526 (2007).
[9]J. H. Kim and K. H. Yoon, J. Mater. Sci.: Mater. Electron. **20**, 879 (2009).
[10]M. Zinkevich and F. Aldinger, J. Am. Chem. Soc. **87**, 683 (2004).
[11]G. Pei, C. Xia, Y. Dong, B. Wu, T. Wang, and J. Xu, Scr. Mater. **58**, 943 (2008).
[12]V. J. Folen, Phys. Rev. **139**, A1961 (1965).
[13]I. G. Kim, T. H. Yeom, S. H. Lee, Y. M. Yu, H. W. Shin, and S. H. Choh, J. Appl. Phys. **89**, 4470 (2001).
[14]A. Wolos, M. Palczewska, M. Zajac, J. Gosk, M. Kaminska, A. Twardowski, M. Bockowski, I. Grzegory, and S. Porowski, Phys. Rev. B **69**, 115210 (2004).
[15]T. Graf, M. Gjukic, M. Hermann, M. S. Brandt, M. Stutzmann, L. Görgens, J. B. Philipp, and O. Ambacher, J. Appl. Phys. **93**, 9697 (2003).
[16]H. Raebiger, S. Lany, and A. Zunger, Phys. Rev. Lett. **101**, 027203 (2008).
[17]F.-X. Jiang, X.-H. Xu, J. Zhang, X.-C. Fan, H.-S. Wu, and G. A. Gehring, Appl. Phys. Lett. **96**, 052503 (2010).
[18]E. G. Víllora, K. Shimamura, Y. Yoshikawa, T. Ujiie, and K. Aoki, Appl. Phys. Lett. **92**, 202120 (2008).
[19]J. L. C. (contact), http://pixe.physics.uoguelph.ca/gupix/about/ Accessed 2010 (2009).
[20]M. Mohamed, C. Janowitz, I. Unger, R. Manzke, Z. Galazka, R. Uecker, R. Fornari, J. R. Weber, J. B. Varley, and C. G. Van de Walle, Appl. Phys. Lett. **97**, 211903 (2010).
[21]J. Perdew, J. Chevary, S. Vosko, K. Jackson, M. Pederson, D. Singh, and C. Fiolhais, Phys. Rev. B **46**, 6671 (1992).
[22]G. Kresse and J. Furthmüller, Phys. Rev. B **54**, 11169 (1996).
[23]G. Kresse and J. Hafner, Phys. Rev. B **47**, 558 (1993).
[24]N. Ueda, H. Hosono, R. Waseda, and H. Kawazoe, Appl. Phys. Lett. **70**, 3561 (1997).
[25]J. J. Kim, H. Makino, M. Sakurai, D. C. Oh, T. Hanada, M. W. Cho, T. Yao, S. Emura, and K. Kobayashi, J. Vac. Sci. Technol. B **23**, 1308 (2005).
[26]A. Titov, X. Biquard, D. Halley, S. Kuroda, E. Bellet-Amalric, H. Mariette, J. Cibert, A. E. Merad, G. Merad, M. B. Kanoun, E. Kulatov, and Y. A. Uspenskii, Phys. Rev. B **72**, 115209 (2005).
[27]C. Kittel, *Introduction to Solid State Physics*, 8th ed. (Wiley, New Jersey, 2005).
[28]T. C. Lovejoy, R. Chen, X. Zheng, E. G. Villora, K. Shimamura, H. Yoshikawa, Y. Yamashita, S. Ueda, K. Kobayashi, S. T. Dunham, F. S. Ohuchi, and M. A. Olmstead, Appl. Phys. Lett. **100**, 181602 (2012).
[29]E. G. Villora, K. Shimamura, T. Ujiie, and K. Aoki, Appl. Phys. Lett. **92**, 202118 (2008).
[30]T. C. Lovejoy, E. N. Yitamben, N. Shamir, J. Morales, E. G. Villora, K. Shimamura, S. Zheng, F. S. Ohuchi, and M. A. Olmstead, Appl. Phys. Lett. **94**, 081906 (2009).
[31]H. H. Tippins, Phys. Rev. **137**, A865 (1965).
[32]D. Vivien, B. Viana, A. Revcolevschi, J. D. Barrie, B. Dunn, P. Nelson, and O. M. Stafsudd, J. Lumin. **39**, 29 (1987).
[33]B. N. Figgis and M. A. Hitchman, *Ligand Field Theory and Its Applications* (Wiley, New York, 1999).
[34]T. Graf, M. Gjukic, M. S. Brandt, M. Stutzmann, and O. Ambacher, Appl. Phys. Lett. **81**, 5159 (2002).
[35]C. G. Van de Walle and J. Neugebauer, J. Appl. Phys. **95**, 3851 (2004).
[36]Multiple Cr-doped samples were grown with comparable doping to the Mn-doped crystal.